Applied Physics Letters

RESEARCH ARTICLE | JULY 31 2024

Acoustically driven ferromagnetic resonance in YIG thin films

Thomas Wong ; Jihun Park ; Kensuke Hayashi ; Miela J. Gross ; Ryan Kim ; Xinjun Wang ; Samuel E. Lofland ; Nathan D. Orloff ; Daniel B. Gopman ; Seunghun Lee ; Paul A. Crowell ; Caroline A. Ross ; Ichiro Takeuchi

Appl. Phys. Lett. 125, 052402 (2024)
https://doi.org/10.1063/5.0211718
CHORUS

AIP Publishing

Applied Physics Letters ARTICLE pubs.aip.org/aip/apl

Acoustically driven ferromagnetic resonance in YIG thin films

Cite as: Appl. Phys. Lett. **125**, 052402 (2024); doi: 10.1063/5.0211718
Submitted: 1 April 2024 · Accepted: 12 July 2024 ·
Published Online: 31 July 2024

Thomas Wong,[1,2] Jihun Park,[2,3] Kensuke Hayashi,[4] Miela J. Gross,[5] Ryan Kim,[3] Xinjun Wang,[3] Samuel E. Lofland,[6] Nathan D. Orloff,[7] Daniel B. Gopman,[8] Seunghun Lee,[9] Paul A. Crowell,[10] Caroline A. Ross,[4] and Ichiro Takeuchi[1,2,3,a)]

AFFILIATIONS

[1]Department of Physics, University of Maryland, College Park, Maryland 20742, USA
[2]Maryland Quantum Materials Center, University of Maryland, College Park, Maryland 20742, USA
[3]Department of Materials Science and Engineering, University of Maryland, College Park, Maryland 20742, USA
[4]Department of Materials Science and Engineering, Massachusetts Institute of Technology, Cambridge, Massachusetts 02139, USA
[5]Department of Electrical Engineering and Computer Science, Massachusetts Institute of Technology, Cambridge, Massachusetts 02139, USA
[6]Department of Physics and Astronomy, Rowan University, Glassboro, New Jersey 08028, USA
[7]Communications Technology Laboratory, National Institute of Standards and Technology, Boulder, Colorado 80305, USA
[8]Materials Science and Engineering Division, National Institute of Standards and Technology, Gaithersburg, Maryland 20899, USA
[9]Department of Physics, Pukyong National University, Busan 48513, Republic of Korea
[10]School of Physics and Astronomy, University of Minnesota, Minneapolis, Minnesota 55455, USA

[a)]**Author to whom correspondence should be addressed:** takeuchi@umd.edu

ABSTRACT

Acoustically driven ferromagnetic resonance (ADFMR) is a platform that enables efficient generation and detection of spin waves via magnetoelastic coupling with surface acoustic waves (SAWs). While previous studies successfully achieved ADFMR in ferromagnetic metals, there are only few reports on ADFMR in magnetic insulators such as yttrium iron garnet ($Y_3Fe_5O_{12}$, YIG) despite more favorable spin wave properties, including low damping and long coherence length. The growth of high-quality YIG films for ADFMR devices is a major challenge due to poor lattice-matching and thermal degradation of the piezoelectric substrates during film crystallization. In this work, we demonstrate ADFMR of YIG thin films on $LiNbO_3$ (LNO) substrates. We employed a SiO_x buffer layer and rapid thermal annealing for crystallization of YIG films with minimal thermal degradation of LNO substrates. Optimized ADFMR device designs and time-gating measurements were used to enhance the ADFMR signal and overcome the intrinsically low magnetoelastic coupling of YIG. YIG films have a polycrystalline structure with an in-plane easy direction due to biaxial stresses induced during cooling after crystallization. The YIG device shows clear ADFMR patterns with maximum absorption for $H \approx 160$ mT parallel to SAW propagation, which is consistent with our simulation results based on existing theoretical models. These results expand possibilities for developing efficient spin wave devices with magnetic insulators.

Increasing demand for high-performance computing requires the development of low-loss electronics. One promising platform for achieving this is through magnonics—the transportation and processing of information via spin waves (magnons).[1–5] To achieve practical applications, magnonic components must be able to efficiently generate, transport, manipulate, and detect magnons. One method of efficiently generating magnons is through magnetoelastic coupling utilizing surface acoustic waves (SAWs), a phenomenon known as acoustically driven ferromagnetic resonance (ADFMR).[6–8] In ADFMR, SAW-induced oscillating strains in a magnetostrictive material create an effective magnetic field, which leads to substantial SAW power absorption when ferromagnetic resonance conditions are satisfied by

applied magnetic fields.[6–10] Consequently, ADFMR shows distinctive angle- and field-dependent SAW absorption patterns. Such ADFMR devices are characterized by low power dissipation due to the use of voltage-controlled interdigitated transducers (IDTs) for SAW launching and detection.[11,12] Additionally, these ADFMR devices can be optimized through modifying IDT dimensions, designs, methods, and materials to improve impedance matching and high-frequency performance.[12–14]

Although previous studies have demonstrated ADFMR in magnetic metals—e.g., Ni, Fe, and FeCo—there are no such reports in a magnetic insulator.[6,15,16] Magnetic insulators are important in magnonics as the lack of mobile electrons results in low damping and improved magnon propagation.[4,5] Among magnetic insulators, yttrium iron garnet ($Y_3Fe_5O_{12}$, YIG) has been reported to have the best known magnonic properties, including the lowest Gilbert damping, narrowest FMR linewidth, and farthest magnon propagation distance.[5] Thus, YIG has been the subject of various magnonic studies, such as nonlinear magnon dynamics, magnonic logic devices, thermally induced magnon generation, and spin pumping in Pt/YIG bilayers.[4,5] Such studies typically use high-quality single-crystal YIG films grown on lattice-matched substrates, such as gadolinium gallium garnet.[4,5,17,18] However, ADFMR devices require the use of piezoelectric substrates such as $LiNbO_3$ (LNO), which have a poor lattice match with YIG, precluding epitaxial growth. Moreover, these piezoelectric substrates easily degrade when exposed to the temperatures (>800 °C) required for YIG crystallization, forming crystal defects such as oxygen vacancies or secondary phases.[19–23] Additionally, YIG and many other magnetic insulators have an intrinsically low magnetostriction coefficient compared to ferromagnetic metals.[24,25] These challenges are a significant hurdle to the study of ADFMR in such magnetic insulators.

In this work, we demonstrate ADFMR in polycrystalline YIG thin films deposited on LNO substrates. A thin (5 nm) SiO_x buffer layer was employed to facilitate growth of YIG and suppress unwanted reactions with LNO during heat treatment.[26] To minimize thermal degradation of LNO, the YIG films were fabricated using room-temperature pulsed laser deposition (PLD) followed by rapid thermal annealing (RTA) for crystallization. To enhance the ADFMR signals of polycrystalline YIG, which are expected to be small due to its low magnetostriction (-2.1×10^{-6}),[25] a split-finger IDT design[13] was used to reduce destructive interference at higher frequencies as well as a time-gating method[11,12] to isolate the SAW signal from spurious electromagnetic signals. The YIG thin film showed angle-dependent ADFMR features, implying the magnetization dynamics of YIG can be manipulated by voltage-controlled SAW.

A 5 nm SiO_x buffer layer was first deposited by radio frequency sputtering on Y-cut LNO substrates (i.e., the substrate is the X–Z plane of the LNO trigonal lattice with in-plane vectors $[\bar{2}110]$ and [0001]) to prevent formation of perovskite phases during crystallization. An amorphous YIG-composition film was then deposited on each substrate by PLD (Neocera[47]) using a YIG ($Y_3Fe_5O_{12}$) target of 99.9% purity. The base pressure of the PLD chamber was ~1 mPa. PLD was done at room temperature under an oxygen partial pressure of 2.7 Pa using a 248 nm KrF laser (COMPex Pro 205, Coherent, USA) with a fluence of 2.1 J/cm^2. Rapid thermal annealing (MILA-5000, Advance Riko) of the amorphous YIG-composition films was then performed at 800 °C for 200 s in air to crystallize the YIG films while minimizing degradation of the LNO substrates. The crystallized YIG films were about 180 nm thick. The crystal structures of the YIG films before and after RTA were analyzed using x-ray diffraction (XRD; X'pert Pro MPD, Malvern Panalytical). Atomic force microscopy (AFM; Dimension 5000-1, Digital Instruments) was used to investigate the surface roughness of the YIG films. Vibrating sample magnetometry (VSM; 7400 Series, Lake Shore) was employed to characterize field-dependent magnetization (M–H) of the YIG films. Field-dependent ferromagnetic resonance (FMR) of the samples was measured using a coplanar waveguide, a lock-in amplifier (SR830, Stanford Research Systems), and a radio frequency generator (83752A, Hewlett Packard). A schematic view of the FMR measurement setup is provided in Fig. S1.

A maskless photolithography system (MLA150, Heidelberg Instruments) was used to fabricate the ADFMR devices with IDTs down to 1 μm resolution. Ion beam etching with Ar gas was employed for YIG film patterning, which was then followed by liftoff of 70 nm thick aluminum IDTs deposited by electron beam evaporation (Nexdep, Angstrom Engineering). The IDTs were designed to excite SAWs along the LNO Z-axis, the preferred propagation direction for Rayleigh-type SAWs in Y-cut LNO.[13] SAW launcher designs were optimized based on ADFMR performance, and the final IDT structure had finger widths of $\approx 1.7\ \mu$m, periodicity $\lambda = 10\ \mu$m, and 50 split-finger pairs. The designs of patterned YIG and a printed circuit board (PCB) for sample mounting were also optimized to reduce SAW insertion loss and maximize ADFMR signals. An automated rotating stage with an electromagnet (angle-controllable to around 1°) was developed for field- and angle-dependent ADFMR measurements. The signal transmission between two IDTs (S_{21}) in the frequency domain was measured via a vector network analyzer (VNA; 83752A, Hewlett Packard) to characterize SAW resonance peaks, including odd harmonics. The ADFMR signals were improved by isolating the SAW transmission signals from electromagnetic interference based on time-gated S_{21} measurements at selected harmonic frequencies using an arbitrary waveform generator (AWG7000, Tektronix) and an oscilloscope (Infiniium 54845a, Agilent).

Figure 1(a) shows XRD patterns for YIG thin films deposited on the LNO substrates before and after the RTA process. An ideal XRD pattern of polycrystalline YIG (space group $Ia\bar{3}d$) is provided as a reference (ICDD No. 04-009-8391). The XRD profile of the as-deposited sample shows no peaks other than those of the LNO substrate, indicating that the film is amorphous or poorly crystalline (small grains). Diffraction peaks corresponding to YIG crystals emerge after heat treatment at 800 °C using RTA. This agrees with earlier studies where amorphous YIG was crystallized at 800 °C.[18,27,28] We estimated the YIG crystallite size (D) along the thickness direction employing the Debye–Scherrer equation[29] $D = K\omega/\beta\cos\theta$, where K = 0.9 is a shape factor, $\omega = 0.154\,18$ nm is the wavelength of Ni-filtered CuK_α x-ray, β is the full width of half maximum of diffraction peaks, and θ is the Bragg angle. The out-of-plane crystallite size of YIG was calculated to be 149 ± 65 nm, in good agreement with the YIG film thickness (≈ 180 nm).

Figure 1(b) shows the surface morphology of the crystallized YIG thin film measured using AFM. The YIG film shows the root mean square (RMS) surface roughness of 1.5 nm, suggesting that the film surface remains smooth after YIG crystallization. The AFM image also illustrates grains and grain boundaries, where the in-plane grain size is estimated to be on the order of 1 μm.

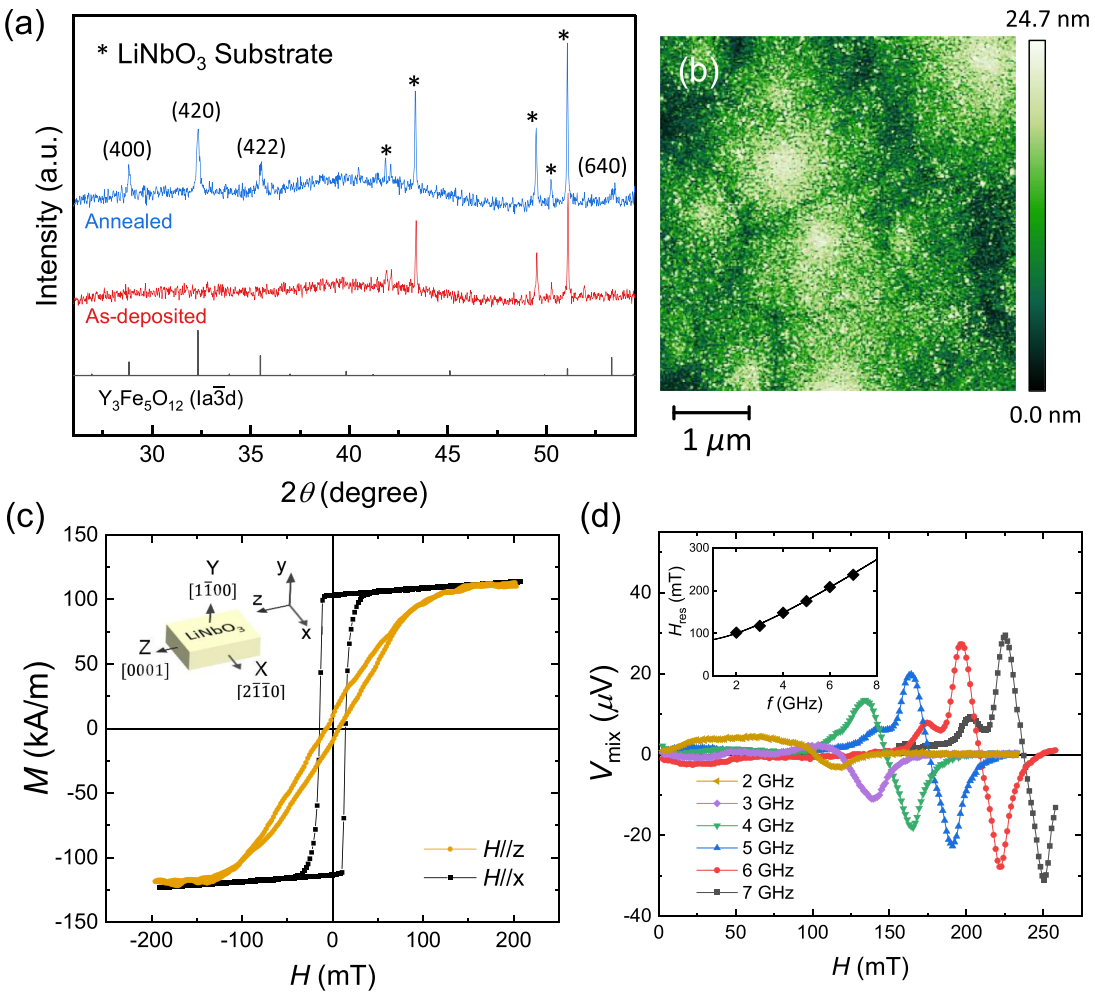

FIG. 1. (a) XRD patterns for YIG/LNO before and after crystallization using RTA. (b) Surface morphology AFM image of YIG after crystallization using RTA. (c) *M*–*H* curves of the YIG thin film with applied fields along the X- and Z-axes. (d) Field-dependent FMR spectra for different excitation frequencies. The inset shows FMR resonance field H_{res} as a function of excitation frequency f for experiments (scatter) and simulations (line). The FMR simulation was performed using the formula $(2\pi f/\gamma)^2 = (H_{res} + H_k - H_{ani})(H_{res} - H_{ani})$, with the gyromagnetic ratio $\gamma/2\pi = 28$ GHz/T, in-plane anisotropy field $H_{ani} = 80$ mT, and out-of-plane anisotropy field $H_k = 230$ mT.

Figure 1(c) shows *M*–*H* curves of a polycrystalline YIG film grown on LNO along X- and Z-axes, defined in the inset figure. The YIG film has a coercive field $H_c \approx 15$ mT and a saturation field $H_s \approx 150$ mT in the Z direction, while in the X direction, $H_c \approx 17$ and $H_s \approx 20$ mT. These values are larger than those of epitaxial YIG films or YIG single crystals,[17,18,27,30] but they are comparable to those of polycrystalline YIG thin films deposited on non-garnet substrates.[28,31,32] The polycrystalline YIG film shows saturation magnetization $M_s \approx 110$ kA/m, which is lower than the bulk value of 140 kA/m but similar to the results of some previous studies on polycrystalline films.[33,34] The observed in-plane magnetic anisotropy of our YIG films can be attributed to anisotropic stresses induced during cooling after RTA due to a mismatch in the coefficients of thermal expansion (CTE) between LNO and YIG. The CTEs of LNO at room temperature along X- and Z-axes are (14.1–16.7)$\times 10^{-6}$ and (2.0 to 7.5)$\times 10^{-6}$ K^{-1}, respectively,[35,36] while that of polycrystalline YIG is 11.2×10^{-6} K^{-1} in all directions.[37] Furthermore, the mismatch in CTE is larger during annealing from RT to 800 °C, resulting in lattice expansions along X- and Z-axes of LNO ($\Delta a = 1.8\%$, $\Delta c = 0.17\%$) and YIG ($\Delta a = \Delta c = 0.8\%$).[36,37] Thus, after cooling the YIG films developed tensile stress in the Z direction and compressive stress in the X direction (Fig. S2). The magnetostriction of polycrystalline YIG may be estimated as $\lambda = 0.4\,\lambda_{100} + 0.6\,\lambda_{111}$ where $\lambda_{100} = -1.3 \times 10^{-6}$ and $\lambda_{111} = -2.7 \times 10^{-6}$, yielding $\lambda = -2.1 \times 10^{-6}$.[25] As shown in Fig. S3, this negative magnetostriction results in an easy magnetization axis in the direction of compressive stress (X-axis) and hard axis in the direction of tensile stress (Z-axis).

Figure 1(d) shows FMR data taken at frequencies from 2 to 7 GHz with an input power of 1 mW. The observed linewidth is about 50 mT at 7 GHz, much larger than that observed for single crystals or epitaxial films.[4] Moreover, satellite peaks can be observed, which is consistent with the FMR resonance modes of polycrystalline YIG

films.[38] We also performed FMR simulations of YIG films, which were consistent with our observations as shown in the inset of Fig. 1(d).

Figure 2(a) shows schematic and microscope images of a YIG ADFMR device. A full-view image of our YIG device is provided in Fig. S4. SAW signals are transmitted from IDT1 to IDT2 along the Z-axis of the LNO with S_{21} scattering parameter, defined as $20\log\frac{V_{IDT2}}{V_{IDT1}}$. We used split-finger IDTs to reduce power loss due to internal SAW reflections, thus improving performance at higher harmonics.[13] The angle between the Z-axis and the applied magnetic field is defined as ϕ. As shown in Fig. 2(b), VNA measurements of S_{21} for a device with $\lambda = 10\,\mu$m reveal two SAW resonance modes corresponding to Rayleigh waves ($f_1 = 340$ and $f_3 = 1020$ MHz) and longitudinal waves ($f'_1 = 740$ and $f'_3 = 2220$ MHz). These values are consistent with the velocities of Z-axis propagating SAWs in LNO, 3400 and 7400 m/s, respectively.[13,39]

The VNA measurement shows significant interference due to electromagnetic coupling between IDTs. For this reason, we performed angle- and field-dependent ADFMR measurements with the third harmonic Rayleigh resonance at 1031 MHz employing a time-gating isolation method.[11,12] Figure S5(a) shows the time-gating measurement allowing for separation between electromagnetic waves (EMWs) and SAW signals owing to difference in the speed of light in air vs the speed of SAWs in LNO. The two-dimensional spectrogram shows apparent isolation of the S_{21} voltage signals of SAWs at the excitation frequency from the EMW interference, as illustrated in Figs. S5(b) and S5(c). Note that the EMW background signal is about 10 times smaller than the SAW (10 dB difference) in both the VNA and time-gating measurements, showing good agreement between two measurements of the same device.

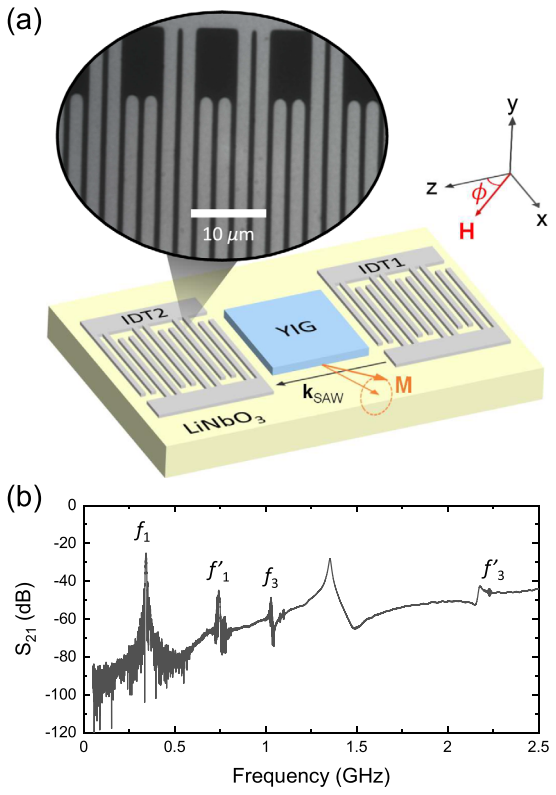

FIG. 2. (a) Schematic view of the YIG/LNO ADFMR device. Inset shows a microscopic image of the IDT split fingers. (b) S_{21} as a function of frequency. Peaks corresponding to SAW absorption (f_1 and f'_1) and the odd harmonics (f_3 and f'_3) are marked.

Figure 3 shows the power absorption of the YIG ADFMR device for different angles. The field-dependent relative power absorption ΔS_{21} for different angles is shown in Fig. 3(a), where ΔS_{21} is normalized to equal 0 dB at high field ($H = 350$ mT). The observed ADFMR features show maximum absorption at $H \approx 160$ mT and $\phi = 0°$. The ADFMR signals reach a maximum absorption of $\Delta S_{21} \approx -0.07$ dB, which are larger than the background noise level (≈0.005 dB). This indicates that the ADFMR of the YIG thin film is sufficient to detect despite the inherently low magnetostriction coefficient of YIG. We performed a thorough quantitative analysis using a theoretical simulation and confirmed that the observed absorption feature is due to ADFMR in YIG films. Detailed description of YIG ADFMR simulation is provided in the supplementary material, including theoretical formula and simulation parameters (Tables S1 and S2). The absorption line profiles obtained via the YIG ADFMR simulation [Fig. 3(b)] are reasonably consistent with the experimental observation [Fig. 3(a)]. The two-dimensional maps of ΔS_{21} as functions of H and ϕ also show good agreement between experiment and simulation, as presented in Figs. 3(c) and 3(d).

For comparison, we measured an ADFMR device with a 20 nm Ni thin film, a ferromagnetic metal studied extensively for ADFMR research, as a reference material. The Ni ADFMR device shows SAW resonance peaks (f_1 and f'_1) and corresponding odd harmonics (f_3 and f_5) (Fig. S6). The Ni ADFMR measured at $f_5 = 1711.9$ MHz shows clear angle dependence with maximum absorption ($\Delta S_{21} \approx -12$ dB) at $\phi = 10°$ and $H = 20$ mT (Fig. S7), which is in good agreement with some previous reports.[6,10,40]

The ADFMR pattern of the YIG device is different from that of the Ni device. One remarkable difference is the ADFMR absorption intensity. The maximum ADFMR absorption for the YIG and Ni devices is ≈−0.07 and ≈−12 dB, respectively. The difference is about 170 times, which is greater than the expected difference (1.7 times) considering the magnetostriction constants of YIG (-2.1×10^{-6})[25] and Ni (-40×10^{-6})[41] in addition to other device parameters, such as material stiffness, thickness, M_s, and operating frequencies (for more details, please see the supplementary material). This discrepancy can be explained by structural effects, such as increased magnetic damping due to film stress, defects, and grain boundaries in the YIG films.[18]

Additionally, it should be noted that the highest SAW excitation frequencies for the YIG and Ni ADFMR devices are different, which could be due to partial thermal degradation of LNO substrates in YIG samples. Despite identical IDT designs and Y-cut LNO substrates, the S_{21} of the third harmonic SAW is much lower and the fifth harmonic Rayleigh wave excitation is not observable in the YIG device. This is attributable to the high-temperature RTA used for the crystallization of YIG, which could have partially degraded the LNO substrate by forming crystal defects, such as oxygen vacancies.[19–23] This degradation of the substrate is supported by the fact that the XRD peaks for the substrate are broadened after annealing, $\beta = (0.060° \pm 0.003°)$ to $(0.065° \pm 0.004°)$.

As shown in Figs. 3(c) and 3(d), our experimental data are consistent with the ADFMR power absorption simulations except for angle-independent absorption observed at low field ($H \leq 50$ mT). This low-

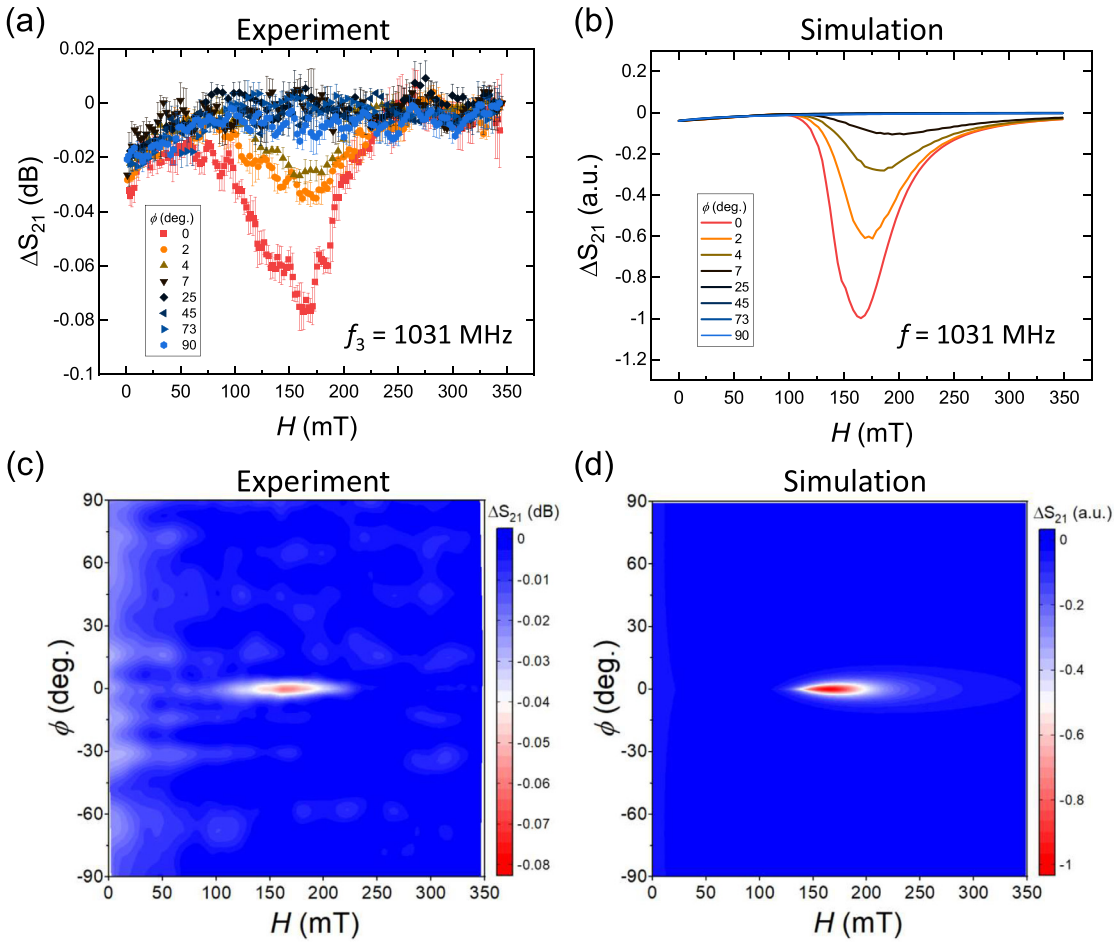

FIG. 3. Power absorption ΔS_{21} as a function of applied field strength for different angles in (a) experiment and (b) simulation. Two-dimensional map of power absorption ΔS_{21} as functions of applied field angle and strength in (c) experiment and (d) simulation.

field absorption can also be observed in the Ni device at $H \leq H_s$ [Figs. S8(a) and S8(b)]. This is likely due to power absorption in unsaturated films occurring when an applied field is smaller than H_s. Similar angle-independent absorption at low applied fields is also seen in previous ADFMR studies.[6,10]

The angle-dependent absorption feature shows discrepancies between the YIG and Ni devices, as the YIG ADFMR power absorption peaks at $\phi = 0°$ rather than increased angles ($\phi \geq 10°$) seen in the Ni ADFMR device. Our YIG ADFMR simulation reveals that the difference is likely due to non-negligible strain components. In previous ADFMR studies, only the ε_{zz} component was considered significant for Z-propagating Rayleigh wave in Y-cut LNO; other strain components were approximated to be zero due to the spatial dimensions of the magnetic thin films. On the other hand, the best matching parameters in our YIG ADFMR simulation include other strain components (ε_{xz}, ε_{xx}, and ε_{yz}) in addition to ε_{zz}. The effective driving field for our YIG ADFMR simulation contains four strain components as follows:[6]

$$\begin{pmatrix} h_1 \\ h_2 \end{pmatrix} = \frac{B}{\mu_0 M_s} \begin{pmatrix} 2\varepsilon_{yz}\cos(\phi_0) \\ (\varepsilon_{zz} - \varepsilon_{xx})\sin(2\phi_0) - 2\varepsilon_{xz}\cos(2\phi_0) \end{pmatrix}, \quad (1)$$

where ε_{ij} are the strain tensor components of the SAW, B is the magnetoelastic coupling constant, and ϕ_0 is the magnetization direction. Note that in the presence of magnetic anisotropy, $\phi_0 \neq \phi$ in general, which we find is the case in our YIG films. See the supplementary material for further details.

The out-of-plane shear strain components (ε_{yz}) of Rayleigh waves become non-negligible when the thin-film approximation is not applicable (i.e., thicker films as in our YIG devices), which induces a driving field h_1 that has a maximum strength at 0°.[6,8,42] As this ε_{yz} contribution increases, the ADFMR power absorption at 0° increases. The in-plane strain components (ε_{xx} and ε_{xz}) become significant when there is dispersed and non-plane wave-like SAW propagation, as reported in a recent ADFMR study of focused IDT devices.[43] Our YIG cells are several times longer (aspect ratio of 6.7) in length than square-shaped Ni cells. Thus, the SAWs in our YIG devices are more likely affected

by in-plane effects, which introduce non-zero ε_{xx} and ε_{xz} components, such as interactions with the YIG grain boundaries and film edges. Additionally, large in-plane magnetic anisotropy in our YIG devices has a significant effect on the angle-dependent features, leading to very narrow ADFMR absorption features around 0°.[44,45] This anisotropy is largely due to film stresses, as it opposes any potential in-plane shape anisotropy that may be caused by our bar-shaped YIG films. When these factors—film thickness, non-trivial SAW propagation, and in-plane magnetic anisotropy—come into play simultaneously, this can result in the observed single-lobe ADFMR pattern. To explain the contributions of each parameter to the power absorption patterns (single-lobe or multiple-lobe), we provide details of our ADFMR simulation in Figs. S9–S12.

To demonstrate ADFMR in YIG, we have attempted to address issues regarding poor substrate match and thermal degradation during film crystallization. Partial substrate degradation in our YIG devices was observed, which likely resulted in reduced ADFMR signals (≈0.07 dB) due to a decreased operating frequency (i.e., absence of the fifth harmonic SAW). Another challenge we encountered lies in in-plane stresses in the YIG films, which can increase damping.[18] The use of a substrate that has lattice constants and temperature-dependent CTEs similar to YIG could allow for the growth of YIG films with less in-plane stresses, thus alleviating this issue. Moreover, a more thermally robust piezoelectric substrate would reduce degradation of SAW performance, which in turn would lead to lower input loss, higher operating frequency, and improved ADFMR signal. One potential candidate for the piezoelectric substrate material of YIG ADFMR is quartz as it has a CTE similar to that of YIG and polycrystalline Ce:YIG films have been grown successfully on Z-cut α-quartz.[46] Our findings would facilitate spin wave device research for low-loss computing applications based on magnetic insulators employing low damping and pure spin wave characteristics.

In this work, ADFMR of YIG thin films was demonstrated. RTA was used to crystallize YIG deposited using PLD with optimized annealing conditions and a thin SiO_x buffer layer to minimize the reaction and degradation of the piezoelectric LNO substrate. Magnetic anisotropy was observed from the angle-dependent *M*–*H* measurements, resulting from the difference in CTE of YIG and LNO. Using time-gating measurements, we detected two key features in our YIG ADFMR devices. A single-lobe ADFMR pattern was observed in the YIG device with maximum absorption at 0°, which was reproduced with theoretical simulation. Different from Ni ADFMR, the ADFMR pattern in our YIG devices can be attributed to non-zero strain components induced by thick films, non-uniform SAW propagation, and stress-induced magnetic anisotropy. These results could pave the path toward the development of magnonic devices based on magnetic insulators.

See the supplementary material for details of the ADFMR simulations, custom-built FMR measurement setup, schematic illustration of film anisotropy induced by CTE difference, angle-dependent magnetic characterization of YIG films, time-gating measurements, angle-dependent *M*–*H* characteristics of Ni thin film, ADFMR features of a Ni/LNO device, and systematic analysis of ADFMR simulation parameters.

This work was supported by the SRC nCORE SMART program (nCORE Task No. 2861.005) and the NIST Cooperative Agreement No. 70NANB23H226 with partial support from AFOSR No. FA9950-22-1-0023 and Laboratory of Physical Sciences. K.H. was funded by JSPS KAKENHI under Grant No. 22J00763. C.A.R. and M.J.G. acknowledge support from NSF Award No. ECCS 2152528. We thank Aaron Hagerstrom for useful discussions.

AUTHOR DECLARATIONS

Conflict of Interest

The authors have no conflicts to disclose.

Author Contributions

Thomas Wong and Jihun Park contributed equally to this work.

Thomas Wong: Data curation (equal); Formal analysis (equal); Investigation (equal); Methodology (equal); Resources (equal); Software (equal); Validation (equal); Visualization (equal); Writing – original draft (equal); Writing – review & editing (equal). **Jihun Park:** Conceptualization (equal); Data curation (equal); Formal analysis (equal); Investigation (equal); Methodology (equal); Project administration (equal); Resources (equal); Software (equal); Validation (equal); Visualization (equal); Writing – original draft (equal); Writing – review & editing (equal). **Kensuke Hayashi:** Data curation (equal); Formal analysis (equal); Funding acquisition (equal); Investigation (equal); Methodology (equal); Resources (equal); Validation (equal); Visualization (equal); Writing – original draft (equal); Writing – review & editing (equal). **Miela J. Gross:** Formal analysis (equal); Funding acquisition (equal); Investigation (equal); Methodology (equal); Resources (lead); Writing – review & editing (supporting). **Ryan Kim:** Data curation (equal); Formal analysis (equal); Investigation (equal); Methodology (equal); Software (equal); Writing – review & editing (equal). **Xinjun Wang:** Conceptualization (equal); Methodology (equal); Resources (equal). **Samuel E. Lofland:** Data curation (equal); Formal analysis (equal); Investigation (equal); Methodology (equal); Resources (equal); Software (equal); Validation (equal); Visualization (equal); Writing – review & editing (equal). **Nathan D. Orloff:** Conceptualization (equal); Resources (equal); Writing – review & editing (equal). **Daniel B. Gopman:** Methodology (equal); Resources (equal); Writing – review & editing (equal). **Seunghun Lee:** Conceptualization (equal); Data curation (equal); Funding acquisition (equal); Methodology (equal); Resources (equal); Writing – review & editing (equal). **Paul A. Crowell:** Conceptualization (equal); Funding acquisition (equal); Methodology (equal); Project administration (equal); Resources (equal); Supervision (equal); Writing – review & editing (equal). **Caroline A. Ross:** Conceptualization (equal); Data curation (equal); Formal analysis (equal); Funding acquisition (equal); Investigation (equal); Methodology (equal); Project administration (equal); Resources (equal); Supervision (equal); Validation (equal); Writing – review & editing (equal). **Ichiro Takeuchi:** Conceptualization (equal); Data curation (equal); Formal analysis (equal); Funding acquisition (equal); Investigation (equal); Methodology (equal); Project administration (equal); Resources (equal); Supervision (equal); Validation (equal); Writing – original draft (equal); Writing – review & editing (equal).

DATA AVAILABILITY

The data that support the findings of this study are available from the corresponding author upon reasonable request.

REFERENCES

[1]P. Pirro, V. I. Vasyuchka, A. A. Serga, and B. Hillebrands, "Advances in coherent magnonics," Nat. Rev. Mater. **6**, 1114 (2021).
[2]A. Barman, G. Gubbiotti, S. Ladak *et al.*, "The 2021 magnonics roadmap," J. Phys. **33**, 413001 (2021).
[3]B. Lenk, H. Ulrichs, F. Garbs, and M. Münzenberg, "The building blocks of magnonics," Phys. Rep. **507**, 107 (2011).
[4]A. V. Chumak, V. I. Vasyuchka, A. A. Serga, and B. Hillebrands, "Magnon spintronics," Nat. Phys. **11**(6), 453 (2015).
[5]A. A. Serga, A. V. Chumak, and B. Hillebrands, "YIG magnonics," J. Phys. D **43**, 264002 (2010).
[6]L. Dreher, M. Weiler, M. Pernpeintner, H. Huebl, R. Gross, M. S. Brandt, and S. T. B. Goennenwein, "Surface acoustic wave driven ferromagnetic resonance in nickel thin films: Theory and experiment," Phys. Rev. B **86**, 134415 (2012).
[7]X. Li, D. Labanowski, S. Salahuddin, and C. S. Lynch, "Spin wave generation by surface acoustic waves," J. Appl. Phys. **122**, 043904 (2017).
[8]P. G. Gowtham, D. Labanowski, and S. Salahuddin, "Mechanical back-action of a spin-wave resonance in a magnetoelastic thin film on a surface acoustic wave," Phys. Rev. B **94**, 014436 (2016).
[9]N. I. Polzikova, S. G. Alekseev, V. A. Luzanov, and A. O. Raevskiy, "Electroacoustic excitation of spin waves and their detection due to the inverse spin Hall effect," Phys. Solid State **60**, 2211 (2018).
[10]M. Weiler, L. Dreher, C. Heeg, H. Huebl, R. Gross, M. S. Brandt, and S. T. B. Goennenwein, "Elastically driven ferromagnetic resonance in nickel thin films," Phys. Rev. Lett. **106**, 117601 (2011).
[11]D. Labanowski, A. Jung, and S. Salahuddin, "Power absorption in acoustically driven ferromagnetic resonance," Appl. Phys. Lett. **108**, 022905 (2016).
[12]D. A. Bas, P. J. Shah, M. E. McConney, and M. R. Page, "Optimization of acoustically-driven ferromagnetic resonance devices," J. Appl. Phys. **126**, 114501 (2019).
[13]M. G. Holland and L. T. Claiborne, "Practical surface acoustic wave devices," Proc. IEEE **62**, 582 (1974).
[14]W. C. Wilson and G. M. Atkinson, "1st order modeling of a SAW delay line using MathCAD," IEEE SoutheastCon 20070016024 (2007).
[15]D. A. Bas, P. J. Shah, A. Matyushov, M. Popov, V. Schell, R. C. Budhani, G. Srinivasan, E. Quandt, N. Sun, and M. R. Page, "Acoustically driven ferromagnetic resonance in diverse ferromagnetic thin films," IEEE Trans. Magn. **57**, 4300605 (2021).
[16]J.-Y. Duquesne, P. Rovillain, C. Hepburn, M. Eddrief, P. Atkinson, A. Anane, R. Ranchal, and M. Marangolo, "Surface-acoustic-wave induced ferromagnetic resonance in fe thin films and magnetic field sensing," Phys. Rev. Appl. **12**, 024042 (2019).
[17]B. Bhoi, N. Venkataramani, S. Prasad, R. P. R. C. Aiyar, G. Kumar, I. Samajdar, and M. Kostylev, "Observation of enhanced magnetic anisotropy in PLD YIG thin film on GGG (1 1 1) substrate," J. Magn. Magn. Mater. **483**, 191 (2019).
[18]B. Bhoi, B. Kim, Y. Kim, M.-K. Kim, J.-H. Lee, and S.-K. Kim, "Stress-induced magnetic properties of PLD-grown high-quality ultrathin YIG films," J. Appl. Phys. **123**, 203902 (2018).
[19]K. L. Sweeney and L. E. Halliburton, "Oxygen vacancies in lithium niobate," Appl. Phys. Lett. **43**, 336 (1983).
[20]M. Sumets, A. Kostyuchenko, V. Ievlev, S. Kannykin, and V. Dybov, "Influence of thermal annealing on structural properties and oxide charge of $LiNbO_3$ films," J. Mater. Sci. **26**, 7853 (2015).
[21]L. A. Kappers, K. L. Sweeney, L. E. Halliburton, and J. H. W. Liaw, "Oxygen vacancies in lithium tantalate," Phys. Rev. B **31**, 6792 (1985).
[22]S. Leontsev, P. J. Shah, H. S. Kum *et al.*, "Functional properties of yttrium iron garnett thin films on graphene-coated $Gd_3Ga_5O_{12}$ for remote epitaxial transfer," J. Magn. Magn. Mater. **556**, 169440 (2022).
[23]P. C. Dorsey, S. E. Bushnell, R. G. Seed, and C. Vittoria, "Epitaxial yttrium iron garnet films grown by pulsed laser deposition," J. Appl. Phys. **74**, 1242 (1993).
[24]J. Atulasimha and A. B. Flatau, "A review of magnetostrictive iron–gallium alloys," Smart Mater. Struct. **20**, 043001 (2011).
[25]A. B. Smith and R. V. Jones, "Magnetostriction constants from ferromagnetic resonance," J. Appl. Phys. **34**, 1283 (1963).
[26]M. J. Gross, W. A. Misba, K. Hayashi, D. Bhattacharya, D. B. Gopman, J. Atulasimha, and C. A. Ross, "Voltage modulated magnetic anisotropy of rare earth iron garnet thin films on a piezoelectric substrate," Appl. Phys. Lett. **121**, 252401 (2022).
[27]R. Kumar, Z. Hossain, and R. C. Budhani, "Effects of post-deposition annealing on the structure and magnetization of PLD grown yttrium iron garnet films," J. Appl. Phys. **121**, 113901 (2017).
[28]A. I. Serokurova, S. A. Sharko, E. N. Galenko, V. A. Ketsko, and M. N. Smirnova, "Submicron iron-garnet films on lithium-niobate substrates obtained by ion-beam deposition," J. Surf. Invest. **15**, 806 (2021).
[29]U. Holzwarth and N. Gibson, "The Scherrer equation versus the 'Debye-Scherrer equation'," Nat. Nanotechnol. **6**, 9 (2011).
[30]S. A. Manuilov, R. Fors, S. I. Khartsev, and A. M. Grishin, "Submicron $Y_3Fe_5O_{12}$ film magnetostatic wave band pass filters," J. Appl. Phys. **105**, 033917 (2009).
[31]A. I. Stognij, N. N. Novitskii, S. A. Sharko, A. I. Serokurova, M. N. Smirnova, and V. A. Ketsko, "Growth and properties of $Y_3Fe_5O_{12}$ films on $LiNbO_3$ substrates," Inorg. Mater. **56**, 847 (2020).
[32]S. Tan, Y. Liu, J. Chen, L. Yang, J. Lan, and B. Dai, "Study on lattice constant and magnetic properties of bismuth substituted YIG polycrystal thin film on different substrates prepared by rf magnetron sputtering," J. Mater. Sci. **30**, 7410 (2019).
[33]B. B. Krichevtsov, S. V. Gastev, S. M. Suturin, V. V. Fedorov, A. M. Korovin, V. E. Bursian, A. G. Banshchikov, M. P. Volkov, M. Tabuchi, and N. S. Sokolov, "Magnetization reversal in YIG/GGG(111) nanoheterostructures grown by laser molecular beam epitaxy," Sci. Technol. Adv. Mater. **18**, 351 (2017).
[34]T. Fakhrul, S. Tazlaru, L. Beran, Y. Zhang, M. Veis, and C. A. Ross, "Magneto-optical Bi:YIG films with high figure of merit for nonreciprocal photonics," Adv. Opt. Mater. **7**, 1900056 (2019).
[35]S. C. Abrahams, H. J. Levinstein, and J. M. Reddy, "Ferroelectric lithium niobate. 5. Polycrystal x-ray diffraction study between 24° and 1200 °C," J. Phys. Chem. Solids **27**, 1019 (1966).
[36]IET, *Properties of Lithium Niobate* (IET, 2002).
[37]S. Geller, G. P. Espinosa, and P. B. Crandall, "Thermal expansion of yttrium and gadolinium iron, gallium and aluminum garnets," J. Appl. Cryst. **2**, 86 (1969).
[38]A. I. Stognij, L. V. Lutsev, V. E. Bursian, and N. N. Novitskii, "Growth and spin-wave properties of thin $Y_3Fe_5O_{12}$ films on Si substrates," J. Appl. Phys. **118**, 023905 (2015).
[39]R. T. Smith and F. S. Welsh, "Temperature dependence of the elastic, piezoelectric, and dielectric constants of lithium tantalate and lithium niobate," J. Appl. Phys. **42**, 2219 (1971).
[40]P. G. Gowtham, T. Moriyama, D. C. Ralph, and R. A. Buhrman, "Traveling surface spin-wave resonance spectroscopy using surface acoustic waves," J. Appl. Phys. **118**, 233910 (2015).
[41]E. Klokholm, "The measurement of magnetostriction in ferromagnetic thin films," IEEE Trans. Magn. **12**, 819 (1976).
[42]M. Küß, M. Heigl, L. Flacke, A. Hörner, M. Weiler, M. Albrecht, and A. Wixforth, "Nonreciprocal Dzyaloshinskii–Moriya magnetoacoustic waves," Phys. Rev. Lett. **125**, 217203 (2020).
[43]P. J. Shah, D. A. Bas, A. Hamadeh, M. Wolf, A. Franson, M. Newburger, P. Pirro, M. Weiler, and M. R. Page, "Symmetry and nonlinearity of spin wave resonance excited by focused surface acoustic waves," Adv. Electron. Mater. **9**, 2300524 (2023).
[44]B. D. Cullity and C. D. Graham, *Introduction to Magnetic Materials*, 2nd ed. (Wiley-IEEE Press, 2008).
[45]G. Wedler, J. Walz, A. Greuer, and R. Koch, "Stress dependence of the magnetoelastic coupling constants $\boldsymbol{B}_1$ and $\boldsymbol{B}_2$ of epitaxial Fe(001)," Phys. Rev. B **60**, R11313 (1999).
[46]X. Y. Sun, Q. Du, T. Goto, M. C. Onbasli, D. H. Kim, N. M. Aimon, J. Hu, and C. A. Ross, "Single-step deposition of cerium-substituted yttrium iron garnet for monolithic on-chip optical isolation," ACS Photonics **2**, 856 (2015).
[47]Certain commercial equipment, instruments, or materials are identified in this document. Such identification does not imply recommendation or endorsement by the National Institute of Standards and Technology, nor does it imply that the products identified are necessarily the best available for the purpose.